First-principles investigation of charged dopants and dopant-vacancy defect complexes in monolayer MoS_2

Anne Marie Z. Tan,[1,2,*] Christoph Freysoldt,[3] and Richard G. Hennig[1,2,†]

[1]*Department of Materials Science and Engineering, University of Florida, Gainesville, FL 32611, USA*
[2]*Quantum Theory Project, University of Florida, Gainesville, FL 32611, USA*
[3]*Max-Planck-Institut für Eisenforschung GmbH, Max-Planck-Straße 1, 40237 Düsseldorf, Germany*

(Dated: October 2, 2020)

Substitutional doping of two-dimensional semiconducting transition metal dichalcogenides such as MoS_2 offers a stable and promising route for tailoring their electrical, optical, and magnetic properties. We perform density functional theory calculations for two promising transition metal dopants, Re and Nb, and their defect complexes with intrinsic S vacancies in MoS_2. We compute the formation energy of each dopant and complex in different charge states utilizing a charge correction scheme that enables us to accurately predict the charge transition levels and complex binding energies, as well as characterize their electronic properties. We predict remarkably different behavior between Re and Nb dopants and their defect complexes: Re dopants can form complexes with S vacancies which quench the *n*-type doping of Re_{Mo}, while Nb dopants are unlikely to form such complexes and their *p*-type doping properties appear to be less sensitive to the presence of S vacancies.

I. INTRODUCTION

In recent years, two-dimensional (2D) semiconductor materials, such as the transition metal dichalcogenides (TMDCs), monochalcogenides, group III-V compounds, and phosphorene, have attracted significant research attention for their potential applications in optoelectronics, spintronics, photovoltaics, and catalysis [1–18]. One of the most promising and well-studied 2D semiconductor materials is the prototypical TMDC material, molybdenum disulfide (MoS_2), which has demonstrated interesting electronic, optical, and mechanical properties, making it a promising candidate for optoelectronic and catalytic applications [1, 2, 19–21]. MoS_2 is commonly reported to be natively *n*-type [2, 22, 23]. However, the origin of this behavior is still uncertain and has been variously attributed to the presence of intrinsic defects such as sulfur vacancies [24–26], interactions with substrates/interfaces [27], or hydrogen impurity adatoms and interstitials [28]. The development of stable, controllable, and efficient methods for large-scale *n*- and *p*-type doping of 2D MoS_2 is critical in order to fully realize its potential for applications in electronic and optoelectronic devices based on 2D materials.

Doping is a well-established technique for tuning the carrier type, concentrations, and mobilities in conventional bulk semiconductors. In recent years, doping is also being investigated as an effective method to tune the electrical, optical, and magnetic properties of 2D semiconductors, including TMDCs [29]. In MoS_2 and other 2D TMDCs, substitutional doping – and in particular transition metal doping on the host transition metal site – has been experimentally realized and offers a stable and promising route for tailoring their properties. For example, rhenium (Re) and niobium (Nb), which respectively have one more and one fewer valence *d*-electron than Mo, have been proposed as potential *n*-type and *p*-type dopants in MoS_2. Re substitutional doping of MoS_2 has been achieved in layered thin films [30], nanoparticles [31], and monolayers [32, 33], and demonstrated to indeed result in *n*-type behavior. Achieving stable and controllable *p*-type doping in MoS_2 has generally been more challenging due to its native *n*-type conductivity. In recent years, however, some studies have reported successful *p*-type doping by substitution of Nb in MoS_2 layered bulk crystals [34], thin films [35], and monolayers [36, 37].

Dopants and point defects can also form defect complexes in semiconductors, which alter the electronic properties than the individual dopants and defects. While they have not yet been widely studied in 2D semiconductors, there have been several studies of dopant-defect complexes in bulk semiconductors such as GaN and AlN [38–42], and MgO [43]. Some dopant-defect complexes are predicted to have unique optical and electronic properties [38, 39, 42, 43], while in some cases, the formation of these complexes has been found to passivate the dopants or act as recombination centers, limiting the doping efficiency [40, 42]. Motivated by these studies of defect complexes in bulk semiconductors, we seek to investigate the energetics and electronic properties of dopant-defect complexes in 2D MoS_2. S vacancies have been predicted [44–46] and experimentally observed [47–50] to be the most common intrinsic defect in MoS_2. We have performed a detailed study of the S vacancy in both monolayer and layered bulk MoS_2 in our previous study [51]; hence this work will not focus on the S vacancy itself but on its interaction with Re and Nb dopants to form dopant-vacancy complexes.

In this work, we study the stability, and electronic and magnetic properties of Re and Nb substitutional dopants and their complexes with S vacancies in single-layer MoS_2. Figure 1 depicts the different types of defects considered in this study: a substitutional dopant on the Mo-site, a S vacancy, and a dopant-vacancy complex. We assume both Re and Nb to be substitutional dopants on the transition metal Mo-site, which has been predicted to be the most energetically favorable site [52], and as has been experimentally observed [53]. We consider the dopant-vacancy complex in which the dopant and S vacancy are first-nearest-neighbors, as illustrated in

* annemarietan@ufl.edu
† rhennig@ufl.edu

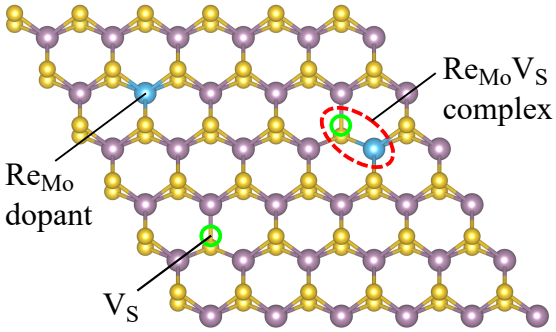

FIG. 1. Schematic showing the types of defects considered in this study: a substitutional dopant on a Mo-site (e.g., Re_{Mo}), a S vacancy (V_S), and a dopant-vacancy complex (e.g., $Re_{Mo}V_S$). Purple, gold, and blue atoms indicate Mo, S, and Re atoms, respectively, while the bright green circle marks the position of the S vacancy. The defects are depicted in the same supercell for illustration purposes only; they are each treated separately in the DFT calculations.

Fig. 1. For each dopant and dopant-vacancy complex, we compute the formation energies, charge transition levels, complex binding energies, and electronic properties, and show that different dopants tend to bind differently to vacancies, giving rise to very different electronic properties.

This paper is organized as follows. In Sec. II, we describe our computational approach and provide details of our density functional theory (DFT) calculations. Sections III and IV present the results for the Re dopant and complex, and Nb dopant and complex, respectively. We compute the formation energies, charge transition levels (CTLs), and electronic properties of both defects and verify the donor (acceptor) characteristics of substitutional Re (Nb) in MoS_2. For the complexes, in addition to computing the formation energies, CTLs, and electronic properties, we also evaluate the binding energy for complex formation. We predict that Re binds strongly to S vacancies, and in doing so, actually passivates the dopant, limiting the effectiveness of Re doping of MoS_2. On the other hand, we find that the Nb dopant is not likely to form $Nb_{Mo}V_S$ complexes, which could make it a robust candidate for $p-$doping MoS_2. We discuss some practical implications of our findings in Sec. V, followed by a summary and conclusions in Sec. VI.

II. COMPUTATIONAL DETAILS

We compute the material and defect properties using density functional theory (DFT) as implemented in the plane-wave code VASP [54]. We use projector-augmented wave (PAW) potentials [55] generated by Kresse and Joubert [56] with valence electron configurations of $4p^6 4d^4 5s^1$, $4p^6 4d^5 5s^1$, $5p^6 5d^5 6s^2$, and $3s^2 3p^4$ to model Nb, Mo, Re, and S, respectively. We treat the exchange-correlation using three different sets of functionals – the Perdew-Burke-Ernzerhof (PBE) [57] generalized gradient approximation (GGA) functional, the strongly constrained and appropriately normed (SCAN) [58] meta-GGA functional, and the hybrid Heyd–Scuseria–Ernzerhof functional HSE06 [59, 60] – and compare the results. For the calculations with SCAN, we also include long-range van der Waals interactions via the SCAN+rVV10 functional [61]. We perform spin-polarized calculations employing a plane-wave cutoff energy of 520 eV, which ensures energy convergence to within 1 meV/atom. To converge the Brillion zone integration to similar accuracy, we use Methfessel-Paxton smearing [62] with a smearing energy width of 0.10 eV and Γ-centered Monkhorst-Pack k-point meshes [63]. For the structural relaxations, we use k-point meshes corresponding to a $12\times12\times1$ k-point mesh per hexagonal unit cell of monolayer MoS_2 (≈ 400 k-points per reciprocal atom in 2D). For the density of states calculations, we double the density of the k-point meshes in all directions and use Gaussian smearing with a reduced smearing width of 0.02 eV. In our previous study of the S vacancy in MoS_2 [51], spin-orbit coupling was found to change the defect formation energies by only 10 to 15 meV and did not qualitatively change our conclusions, therefore, we do not consider the effect of spin-orbit coupling in this study.

We model the defective systems by constructing $3\times3\times1$, $4\times4\times1$, and $5\times5\times1$ supercells based on the hexagonal primitive unit cell, varying the amount of vacuum spacing between layers to be 10, 15, or 20 Å, and replacing and removing atoms accordingly to create substitutional and vacancy defects. We fix the supercell lattice vectors for all defect structures to the equilibrium lattice constant, $a_0 = 3.166$ Å, obtained with the SCAN+rvv10 functional [51] and perform the atomic relaxations using the conjugate gradient algorithm. Calculations utilizing the HSE06 functional are significantly more computationally expensive; hence we only carry out single-point calculations at the PBE-relaxed structures in $3\times3\times1$ supercells. In these smaller supercells, the wavefunctions of shallow defect states may not be sufficiently localized, and the overlap between defect wavefunctions can lead to incorrect electronic ground states with fractional occupancies of bands, which is unphysical in a semiconductor. To avoid this, we fix the band occupancies during these calculations in the small supercells at integer occupancies, which reproduce the ground state electronic structures found using the large supercells [64].

The formation energy $E^f[X^q]$ of a point defect X with charge q is determined from DFT calculations using a supercell approach following

$$E^f[X^q] = E_{\text{tot}}[X^q] - E_{\text{tot}}[\text{pristine}] - \sum_i n_i\mu_i + qE_{\text{F}} + E_{\text{corr}}, \quad (1)$$

where $E_{\text{tot}}[X^q]$ and $E_{\text{tot}}[\text{pristine}]$ are the total DFT-derived energies of the supercell containing the defect X and the pristine supercell, respectively, n_i is the number of atoms of species i added/removed by the defect, μ_i is the corresponding chemical potential of the species, and E_{F} is the Fermi energy. In this work, we consider the Mo-rich/S-poor limit, for which the appropriate S chemical potential $\mu_S(\text{S-poor}) = (\mu_{MoS_2} - \mu_{Mo(bcc)})/2$. The chemical potentials for Re and Nb are referenced to the bulk hcp Re and bcc Nb phases, respectively.

The final term in Eq. (1), E_{corr}, contains corrections to the formation energy due to electrostatic interactions with periodic images and the implicit compensating background charges, which are introduced in supercell calculations using plane-wave DFT approaches. Modeling charged defects in single-layer materials is particularly challenging because the uniform compensating background charge results in a quadratic potential across the vacuum, which leads to the unphysical divergence of the energy with vacuum spacing. In this work, we apply the correction scheme developed recently by Freysoldt and Neugebauer [65], which employs a surrogate model to restore the appropriate electrostatic boundary conditions for charged 2D materials to accurately compute the formation energies of dopants and dopant-vacancy complexes in monolayer MoS_2. The effectiveness of this charge correction scheme has been demonstrated in our previous study of S vacancies in MoS_2 [51]. The correction scheme also works well when applied to charged dopants and complexes – we verify that the corrected defect formation energies are well converged to within less than 100 meV across all supercell sizes. For the calculations with PBE and SCAN+rVV10 functionals, we utilize the formation energies from the largest supercells ($5\times5\times1$) and the 20 Å vacuum spacing in our analysis. Since we only performed the calculations with HSE06 functional in the $3 \times 3 \times 1$ supercells, we assume that the in-plane supercell size dependence due to the elastic interactions between defects would be similar to that when evaluated with PBE and extrapolate the HSE06 defect formation energies accordingly.

A key input to the Freysoldt-Neugebauer charge correction scheme is the dielectric profile of the monolayer. The surrogate model assumes an isotropic dielectric slab; while this may not strictly be valid for a monolayer, the simplified dielectric model correctly reproduces the asymptotic screening properties of the repeated slab system. We compute the static dielectric tensor – including both electronic and ionic contributions – within DFT for a system comprising the monolayer surrounded by vacuum and estimate the monolayer's averaged dielectric constant following the approach detailed in Refs. [51, 66] to be 17.2, 16.3, and 15.9 computed with the PBE, SCAN+rVV10, and HSE06 functional, respectively.

We consider the following reaction for the formation of the dopant-vacancy defect complexes:

$$\mathrm{D}_{\mathrm{Mo}}^{q} + \mathrm{V}_{\mathrm{S}}^{q'} - (q'' - q' - q)\, e^{-} \overset{\Delta E}{\rightleftharpoons} (\mathrm{D}_{\mathrm{Mo}}\mathrm{V}_{\mathrm{S}})^{q''}, \qquad (2)$$

where, in the context of this work, the dopant D = Nb or Re, and $\mathrm{V_S}$ is the S vacancy. The q, q', and q'' denote the charge states of the dopant, vacancy, and complex, respectively, and e^- is a single electronic charge. The formation of a defect complex is a grand canonical process. If $q + q' > q''$, electron(s) must be captured from the electron reservoir to form the complex; if $q + q' < q''$, electron(s) are released to the electron reservoir. The binding energy of the defect complex, ΔE, is defined as

$$\Delta E = E^f[(\mathrm{D}_{\mathrm{Mo}}\mathrm{V}_{\mathrm{S}})^{q''}] - E^f[\mathrm{D}_{\mathrm{Mo}}^{q}] - E^f[\mathrm{V}_{\mathrm{S}}^{q'}], \qquad (3)$$

for which a negative ΔE indicates attractive binding. By substituting Eq. (1) into Eq. (3), we can see that unlike the formation energies, ΔE is independent of the chemical potentials of the species involved. However, ΔE does depend on E_{F} with $d(\Delta E)/dE_{\mathrm{F}} = q'' - q' - q$. This value will be non-zero when the formation of the defect complex requires the exchange of electron(s) with the electron reservoir, which has energy E_{F}.

If we assume that the formation of the complex as described by (2) is an equilibrium reaction, the binding energy ΔE determines the relative concentrations of the complexes and individual dopants/defects in a system according to the following expression for the equilibrium constant, K:

$$K = \frac{[\mathrm{D}_{\mathrm{Mo}}\mathrm{V}_{\mathrm{S}}]}{[\mathrm{D}_{\mathrm{Mo}}][\mathrm{V}_{\mathrm{S}}]} = \exp(-\Delta E/k_B T), \qquad (4)$$

where $[X_Y]$ indicates the mole fraction of species X on the respective site Y. Note that $[\mathrm{D}_{\mathrm{Mo}}\mathrm{V}_{\mathrm{S}}]$ and $[\mathrm{D}_{\mathrm{Mo}}]$ are not independent quantities, i.e., $[\mathrm{D}_{\mathrm{Mo}}\mathrm{V}_{\mathrm{S}}] + [\mathrm{D}_{\mathrm{Mo}}]$ equals the total dopant concentration, which is usually fixed by the experimental growth conditions. The equilibrium concentration of a defect X at temperature T can be estimated from its formation energy:

$$[X]_{\mathrm{eq}} = \exp(-G^f[X]/k_B T) \approx \exp(-E^f[X]/k_B T). \qquad (5)$$

By ignoring degeneracy factors in the prefactor, we obtain the defect concentration in terms of the fraction of possible defect sites that are defects. For a rough estimate, we assume that the electronic and vibrational entropy contributions to the Gibbs energy of formation $G^f[X]$ are small, therefore $G^f[X] \approx E^f[X]$.

III. RHENIUM DOPANT AND DOPANT-VACANCY COMPLEX

A. Energetic stability of defects and complexes

Figure 2(a) shows the defect formation energies of $\mathrm{Re_{Mo}V_S}$, $\mathrm{Re_{Mo}}$, and $\mathrm{V_S}$ in monolayer MoS_2 as a function of the Fermi energy, calculated with the PBE, SCAN+rVV10, and HSE06 functionals. The kinks in the formation energy plots indicate charge transition levels (CTLs), which correspond to the positions of defect states within the bandgap. The +1/0 CTLs are associated with donor states, e.g., a neutral defect loses an electron to become positively charged, while the 0/−1 CTLs are associated with acceptor states, e.g., a neutral defect gains an electron to become negatively charged. The defect formation energies and CTLs predicted by all three functionals for the $\mathrm{V_S}$, $\mathrm{Re_{Mo}}$ dopant, and $\mathrm{Re_{Mo}V_S}$ complex are in generally good agreement with one another and qualitatively lead to the same conclusions. The $\mathrm{Re_{Mo}}$ dopant has a +1/0 CTL, i.e., a donor state, closer to the conduction band minimum (CBM), indicating its potential to be an n-type dopant in MoS_2. However, in the $\mathrm{Re_{Mo}V_S}$ dopant-vacancy complex, the +1/0 CTL is closer to the valance band maximum (VBM) instead, making it a deep donor state. The $\mathrm{Re_{Mo}V_S}$ complex also has a 0/−1 CTL close to the CBM, similar to the $\mathrm{V_S}$ case, which is a deep acceptor state. Therefore, our results suggest that the formation of the $\mathrm{Re_{Mo}V_S}$ complex passivates the n-type doping of

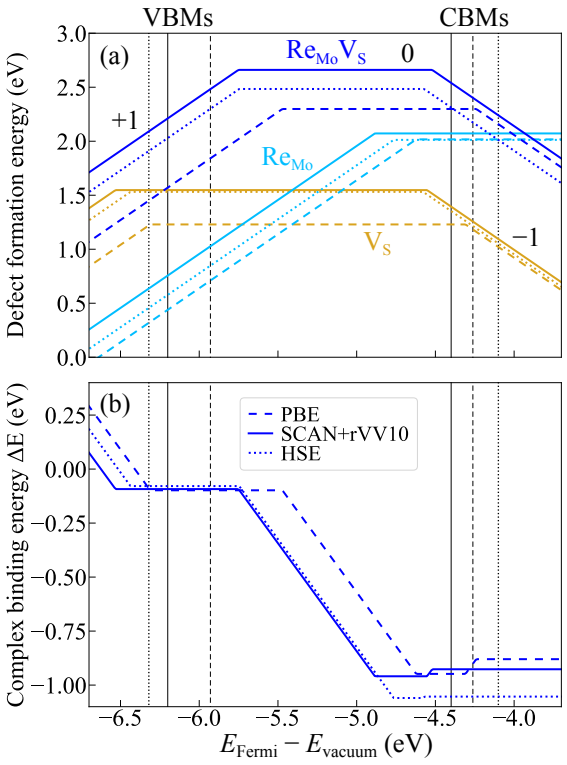

FIG. 2. (a) Defect formation energies of $Re_{Mo}V_S$ (dark blue), Re_{Mo} (light blue), and V_S (gold) in monolayer MoS_2 as a function of the Fermi energy, calculated with PBE (dashed lines), SCAN+rVV10 (solid lines), and HSE06 (dotted lines). The formation energies are computed for S-poor (Mo-rich) and Re-rich conditions. The slopes of the line segments, which correspond to the defect's stable charge state over that range of energies, are indicated on the plot. The black vertical dashed/solid/dotted lines indicate the valence and conduction band edge positions relative to the vacuum level, evaluated using each corresponding functional. (b) Binding energy ΔE for forming the $Re_{Mo}V_S$ complex as a function of the Fermi energy. The ΔE is negative across the gap, indicating attractive binding of up to 1 eV close to the CBM.

the Re dopant by removing the shallow donor state, potentially limiting the effectiveness of the Re dopant in MoS_2.

Figure 2(b) shows that the binding energy ΔE for forming the $Re_{Mo}V_S$ complex from the isolated Re_{Mo} and V_S defects is negative, suggesting that the formation of the defect complex is *energetically* favorable. The binding energy ΔE is computed for the $Re_{Mo}V_S$ complex following Eq. (3) and shows a similar trend when computed with either the PBE, SCAN+rVV10, or HSE06 functional. The binding energy is attractive for all E_{Fermi} within the bandgap, with binding strength varying from around 0.1 eV near the VBM to almost 1 eV close to the CBM. The slopes in the binding energy plot indicate ranges of E_{Fermi} for which the formation of the complex involves an exchange of electrons with the charge reservoir, which has the energy E_{Fermi}. A recent DFT study by Gupta *et al.* reports an attractive binding energy of 0.79 eV for forming the neutral $Re_{Mo}V_S$ complex from neutral Re_{Mo} and V_S [67], which agrees reasonably well with our results. However, as is evident from Fig. 2, there is only a small range of energies over which all three defects are energetically favored to be in the neutral state, and hence only a small set of conditions under which the analysis based only on neutral defects is applicable. By considering each of the defects in multiple charge states, we are able to compute the binding energy as a function of the Fermi level, thereby providing a more complete picture of the defect energetics in this system.

Based on our computed defect formation energies, the equilibrium concentrations of the isolated Re_{Mo} and V_S defects at 750°C (1023 K) can be estimated based on Eq. (5) to be in the approximate ranges of 10^{-10} to 10^{-4} at.% (10^5 to 10^{11} cm^{-2}) and 10^{-8} to 10^{-7} at.% (10^7 to 10^8 cm^{-2}), respectively, which would make it virtually impossible for defect complexes to form regardless of the negative ΔE. However, dopants are intentionally introduced at much higher concentrations (up to few at%), and much higher non-equilibrium concentrations of defects (on the order of 10^{13} cm^{-2} [49, 50]) are often present in these materials as well due to processing techniques, which could create conditions favoring the formation of the defect complexes. Migration barriers for the diffusion of S vacancies in monolayer MoS_2 have been computed with DFT to be greater than 2.0 eV [68, 69]. At high temperature synthesis conditions (≈ 1000 K) and high dopant concentrations (≈ 1 at%), S vacancies can diffuse sufficiently far to be trapped by a dopant. However, at lower temperatures, it would be unlikely for defect complexes to form via diffusion of existing S vacancies or dopants. In both cases, new S vacancies may preferentially form next to existing Re dopants due to the attractive binding energy, thus creating new complexes.

In fact, $Re_{Mo}V_S$ complexes have recently been directly observed via high-angle annular dark-field scanning transmission electron microscopy (HAADF-STEM) of Re-doped monolayer MoS_2 samples grown by chemical vapor deposition (CVD) [70]. Based on their statistics, in a sample with an overall dopant concentration of 1 at.%, Re_{Mo} dopants were observed individually ≈ 94% of the time, while the remaining ≈ 6% of Re dopants were observed in $Re_{Mo}V_S$ complexes. They also reported that the concentration of individual V_S in their sample was ≈ 0.15% in terms of S sites. Based on these reported defect concentrations, at the CVD growth temperature of 750°C, we estimate using Eq. (4) that the binding energy required to give rise to the observed distribution of defects is ≈ −0.33 eV, which falls within the range of values we predict, thus validating our calculations.

B. Electronic structures of defects and complexes

Figures 3(a-b) and 4(a-f) show the projected densities of states for the +1 and neutral individual Re dopant and the +1, neutral, and −1 $Re_{Mo}V_S$ defect complex, respectively. The densities of states are projected onto the *d*-orbitals of the Re dopant, and in the case of the defect complex, also onto the *d*-orbitals of the other two Mo atoms around the S vacancy. Figures 3(c) and 4(g)–(h) depict the charge density of the orbitals corresponding to selected defect peaks of interest, as indicated on the projected density of states plots. In addition, simulated

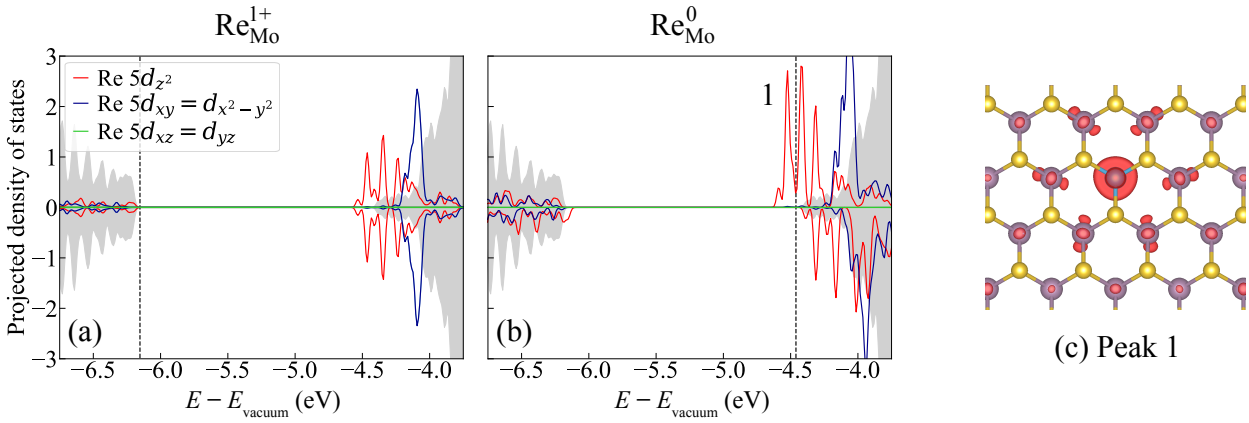

FIG. 3. Projected densities of states for the Re_{Mo} dopant in the (a) +1 and (b) 0 charge states, calculated with the SCAN+rVV10 functional. The densities of states are projected onto the d-orbitals of the Re substitutional dopant atom. For comparison, the total density of states of pristine MoS_2 is shown in grey shading. The energies are plotted with respect to the vacuum energy, with the Fermi energy indicated by the vertical dashed line. Re has one more valence electron than Mo, and in the neutral state, this additional electron occupies a shallow donor defect state close to the CBM, which has d_{z^2} (red) orbital character. The charge density of the orbital corresponding to this defect peak marked "1" is shown in (c). Purple, gold, and blue atoms indicate Mo, S, and Re atoms, respectively.

scanning tunneling microscopy (STM) images of the peaks depicted in 4(g)–(h) are also shown in 4(i)–(j), respectively.

The Re dopant. The projected density of states for the neutral Re dopant (Re^0_{Mo}) in Fig. 3(b) clearly shows a shallow donor state just below the CBM, corresponding to the +1/0 CTL in Fig. 2(a). We emphasize that the positions of defect states are not expected to agree quantitatively with the CTLs since the methods used to evaluate them within DFT differ. The density of states is calculated based on single-particle energies and does not include all many-body exchange and correlation contributions to the energy, which can shift the energies of the defect states. The defect formation energies and CTLs, on the other hand, are evaluated based on differences of total energies for differently charged defect configurations and do include the many-body contributions. Therefore, the CTLs provide a more accurate estimate than the defect levels in density of states or band structure calculations. Previous DFT studies analyzed the density of states of the neutral Re dopant [52, 53, 71] and identified a very shallow dopant donor states just below the CBM, similar to the density of states in Fig. 3(b). In contrast, Komsa *et al.* [45] calculated the CTLs with the scaling approach and found that the donor state is 0.22 eV below the CBM, in close agreement with our results shown in Fig. 2(a).

In defect-free MoS_2, the Mo atoms have trigonal prismatic D_{3h} symmetry, which gives rise to the following crystal field splitting of the d-orbitals: d_{z^2} (a'_1 orbital) < $d_{x^2-y^2} = d_{xy}$ (e' orbitals) < $d_{xz} = d_{yz}$ (e'' orbitals). The presence of an individual substitutional Re dopant preserves that symmetry and orbital degeneracy for the dopant atom, as reflected in the overlapping $d_{x^2-y^2}$ and d_{xy} (blue) and d_{xz} and d_{yz} (green) states in the projected density of states in Figs. 3(a-b). The shallow donor state has d_{z^2} (red) orbital character and gives rise to a local magnetic moment around the neutral dopant atom. However, once the Re atom donates this electron, the dopant becomes positively charged (Re^{1+}_{Mo}), and the net magnetic moment becomes zero.

The Re dopant-vacancy complex. The projected densities of states for the $Re_{Mo}V_S$ defect complex depicted in Fig. 4 indicate the presence of multiple mid-gap states, in stark contrast to what we see for the individual Re dopant in Fig. 3 but similar to the results of our previous study of the S vacancy [51]. The positively charged $(Re_{Mo}V_S)^{1+}$ complex is isoelectronic with the neutral S vacancy, and, similar to the neutral S vacancy, has empty defect states in the gap with primarily $d_{x^2-y^2}$ and d_{xy} orbital character. However, unlike the neutral S vacancy which retains the three-fold symmetry, replacing one of the Mo atoms around the S vacancy by a Re atom breaks that symmetry, lifting the degeneracy between the $d_{x^2-y^2}$ and d_{xy} orbitals. As a result, the defect state is split into two peaks (marked "1" and "2" in Figs. 4(a) and (d)) about 150–200 meV apart in energy, with the lower energy Peak 1 having a greater contribution from the $d_{x^2-y^2}$ orbitals and the higher energy Peak 2 having a greater contribution from the d_{xy} orbitals. This symmetry breaking is also reflected in the shapes of the corresponding defect orbitals shown in Figs. 4(g) and (h).

In addition to plotting the charge isosurfaces, we also depict simulated STM images for these same defect peaks in Fig. 4(i)–(j). Such simulated images can be compared against experimental STM dI/dV maps to verify the nature of the observed dopants and defects [72]. The main feature that distinguishes the complex from the individual dopant is the broken threefold symmetry around the complex, which is clearly observable in the STM images. In addition, by varying the STM bias voltage, one could probe either of the mid-gap defect states, which have noticeably different orbital character. Hence, this is one way how DFT-computed defect properties can assist the assigment of experimental features, and when used in conjunction with each other, provide additional insight into the types and electronic properties of dopants, defects, and complexes present in such samples.

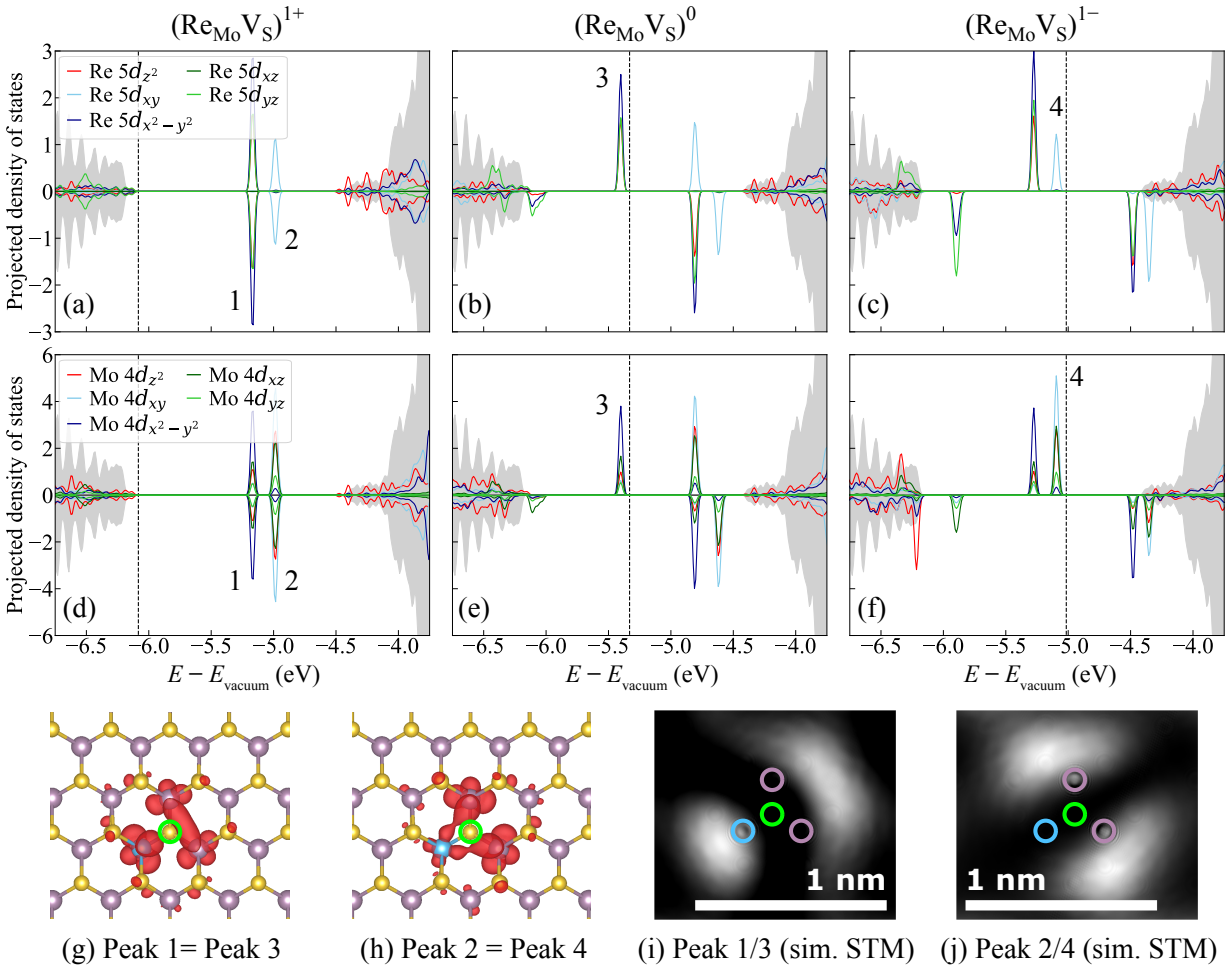

FIG. 4. Projected densities of states for the $Re_{Mo}V_S$ defect complex in the +1, 0, and −1 charge states, calculated with the SCAN+rVV10 functional. The densities of states are projected onto the *d*-orbitals of the Re substitutional dopant atom ((a) – (c)) and *d*-orbitals of the other two Mo atoms directly adjacent to the S vacancy ((d) – (f)). For comparison, the total density of states of pristine MoS_2 is shown in grey shading. The energies are plotted with respect to the vacuum energy, with the Fermi energy indicated by the vertical dashed line. The charge density of the orbitals corresponding to the defect peaks marked "1" – "4" are depicted in (g) and (h), while simulated STM images of the same peaks are shown in (i) and (j). Purple, gold, and blue atoms indicate Mo, S, and Re atoms, respectively, while the bright green circle marks the position of the S vacancy. Purple and blue circles have also been overlaid on the simulated STM images to indicate the positions of the underlying Mo and Re atoms around the defect.

When an electron is added to the positively-charged defect complex to form the neutral complex $(Re_{Mo}V_S)^0$, it becomes isoelectronic to the −1 S vacancy. Since the symmetry breaking of the defect complex lifts the orbital degeneracies and splits the defect states, the additional electron occupies an empty low-energy state in one of the spin channels, resulting in a local net magnetic moment of $1\mu_B$, which is localized on the Re atom and the two Mo atoms next to the vacancy. Interestingly, when another electron is added to form the negatively-charged complex $(Re_{Mo}V_S)^{1-}$, we find that the high-spin state is favored over the low-spin state, resulting in a local net magnetic moment of $2\mu_B$. This implies that in this system, the exchange splitting – the repulsion between electrons of opposite spin in the same orbital (Hund's rule) – is greater than the crystal field splitting – the energy difference between the $d_{x^2-y^2}$ and d_{xy} orbitals.

IV. NIOBIUM DOPANT AND DOPANT-VACANCY COMPLEX

A. Energetics

Figure 5(a) shows the defect formation energies of $Nb_{Mo}V_S$, Nb_{Mo}, and V_S in monolayer MoS_2 as a function of the Fermi energy, calculated with the PBE, SCAN+rVV10, and HSE06 functionals. Once again, all three functionals predict defect formation energies and CTLs for the Nb_{Mo} dopant and $Nb_{Mo}V_S$ complex which are consistent with one another. The Nb_{Mo} dopant has a 0/−1 CTL, i.e., an acceptor state, about 0.5 eV above the valence band maximum (VBM), indicating its potential to be a *p*-type dopant in MoS_2, as expected based on the fact that Nb has one fewer valence electron than Mo. The $Nb_{Mo}V_S$ complex also exhibits a 0/−1 CTL within the

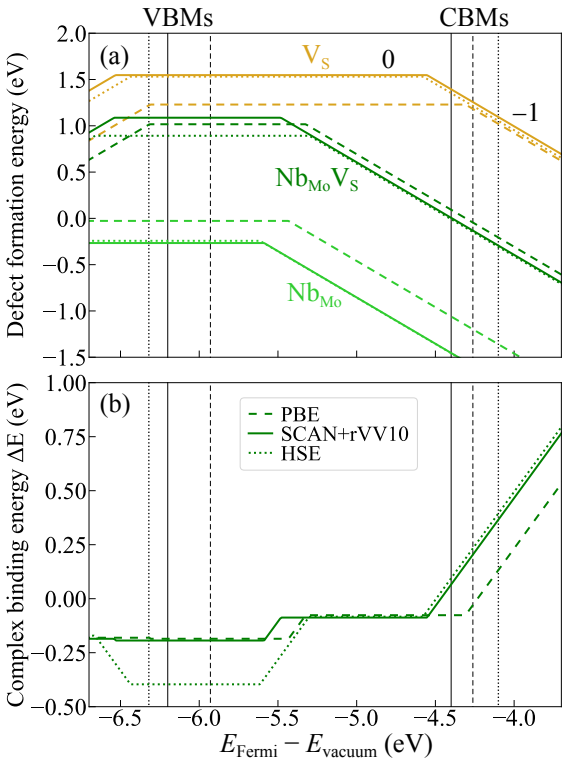

FIG. 5. (a) Defect formation energies of $Nb_{Mo}V_S$ (dark green), Nb_{Mo} (light green), and V_S (gold) in monolayer MoS_2 as a function of the Fermi energy, calculated with PBE (dashed lines), SCAN+rVV10 (solid lines), and HSE06 (dotted lines). The formation energies are computed for S-poor (Mo-rich) and Nb-rich conditions. The slopes of the line segments, which correspond to the defect's stable charge state over that range of energies, are indicated on the plot. The black vertical dashed/solid/dotted lines indicate the valence and conduction band edge positions relative to the vacuum level, evaluated using each corresponding functional. (b) Binding energy ΔE for forming the $Nb_{Mo}V_S$ complex as a function of the Fermi energy. The ΔE is close to zero across the gap, indicating that the individual defects are neither strongly attracted nor repelled from each other.

bandgap, at a similar position as the 0/−1 CTL of the individual Nb_{Mo} dopant. This suggests that, unlike the $Re_{Mo}V_S$ complexes, the formation of $Nb_{Mo}V_S$ complexes may not drastically alter the electronic properties of Nb_{Mo} dopants in MoS_2.

Figure 5(b) shows that the binding energy ΔE for forming the $Nb_{Mo}V_S$ complex from the isolated Nb_{Mo} and V_S defects is only slightly negative for values of E_{Fermi} spanning the bandgap. This suggests that the individual defects are neither strongly attracted nor repelled from each other, again in contrast to the behavior of the Re dopants, which appear to have a significant driving force towards the formation of complexes with S vacancies. The $Nb_{Mo}V_S$ binding energy varies only slightly across the bandgap, changing from around −0.2 eV near the VBM to about zero at the CBM. These results suggest that, unlike the Re dopant, the Nb dopant appears to be more robust against compensation by S vacancies. Not only are the Nb dopant and S vacancy much less likely to form complexes; even if they do, the complex appears to retain similar electronic properties as the individual Nb dopant, which may enable it to still act as an acceptor in MoS_2.

B. Electronic structures

Figures 6(a)–(b) and 7(a)–(f) show the projected densities of states for the neutral and −1 charged Nb dopant and the +1, neutral, and −1 $Nb_{Mo}V_S$ defect complex, respectively. The densities of states are projected onto the *d*-orbitals of the Nb dopant, and in the case of the defect complex, also the *d*-orbitals of the other two Mo atoms around the S vacancy. Figures 6(c) and 7(g)–(j) illustrate the electronic orbitals corresponding to selected defect peaks of interest, as indicated on the projected density of states plots.

The Nb dopant. The projected density of states for the neutral Nb dopant (Nb^0_{Mo}) clearly shows the existence of an acceptor state just above the VBM, as has also been predicted by other DFT studies [37, 71]. This acceptor state which corresponds to the 0/−1 CTL in Fig. 5(a), has d_{z^2} orbital character and gives rise to a local magnetic moment around the neutral Nb dopant. The addition of an electron to this defect state results in the negatively charged Nb dopant Nb^{1-}_{Mo}, which does not have a net magnetic moment. As in the case of the individual Re dopant, the Nb dopant retains the three-fold symmetry and corresponding orbital degeneracy. Hence, we again see that the $d_{x^2-y^2}$ and d_{xy} as well as the d_{xz} and d_{yz} states in the projected density of states overlap.

The Nb dopant-vacancy complex. The projected densities of states for the $Nb_{Mo}V_S$ defect complex depicted in Fig. 7 suggest the existence of multiple defect states within the bandgap. The defect peaks marked "1" and "2" are associated with the +1/0 and 0/−1 CTLs, respectively. By inspecting the orbitals associated with each defect peak, we identify that the defect state associated with the +1/0 CTL in the complex (Fig. 7(g)) has similar character to the defect state of the Nb dopant (Fig. 6(c)), while the state associated with the 0/−1 CTL in the complex (Fig. 7 (h)) has similar character to one of the defect states of the S vacancy [51]. Hence, even though both the individual Nb dopant as well as the Nb-vacancy complex have 0/−1 CTLs within the gap, they have different orbital characters. The defect peaks marked "3" and "4" also exhibit a similar character as the S vacancy defect states, but while they appear towards the top of the bandgap in the density of states calculations, their associated CTLs (−1/−2, −2/−3, etc.) fall deep within the conduction band region based on our defect formation energy calculations. This apparent discrepancy in the positions of defect states is, as mentioned previously, due to the different methods and approximations used to evaluate the CTLs and density of states.

V. DISCUSSION

We find that the different choices of exchange-correlation functional neither significantly alter the defect formation energies nor absolute positions of the CTLs relative to the common vacuum reference for all the defects considered in this

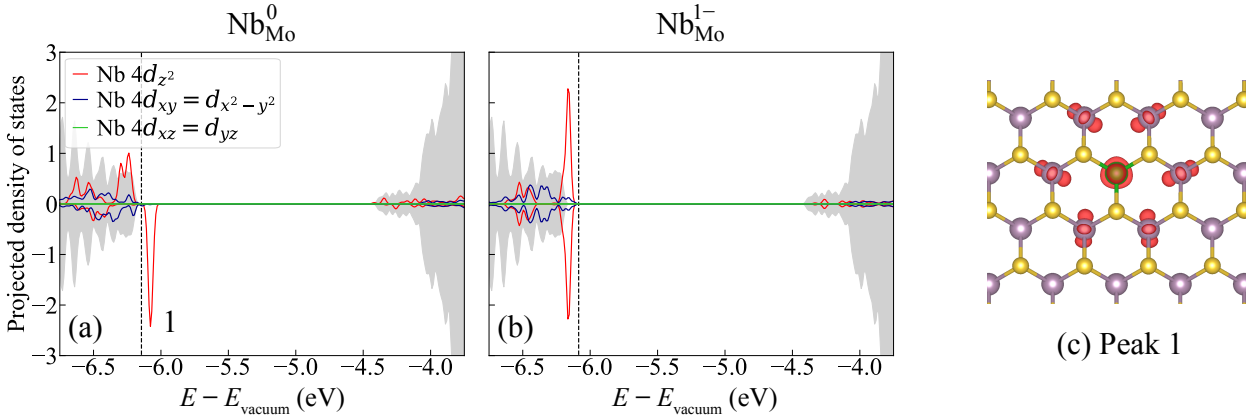

FIG. 6. Projected densities of states for the Nb_{Mo} dopant in (a) 0 and (b) −1 charge states, calculated with the SCAN+rVV10 functional. The densities of states are projected onto the *d*-orbitals of the Nb substitutional dopant atom. For comparison, the total density of states of pristine MoS_2 is shown in grey shading. The energies are plotted with respect to the vacuum energy, with the Fermi energy indicated by the vertical dashed line. Nb has one fewer valence electron than Mo, and in the neutral state, there is an empty shallow acceptor state with d_{z^2} (red) character at the top of the valence band. The charge density of the orbital corresponding to this defect peak marked "1" is depicted in (c). Purple, gold, and green atoms indicate Mo, S, and Nb atoms, respectively.

study. Our finding agrees with a previous study on intrinsic defects in monolayer MoS_2 [45]. The more significant impact of the different exchange-correlation functionals lies in their effect on the bandgap and band edge positions; a posteriori correction schemes for band alignment [73, 74] combined with the current charge correction scheme could provide more accurate estimates of the CTLs. The excellent agreement for the defect formation energy in semilocal and hybrid exchange-correlation functionals validates the accuracy of the DFT predictions. This observation contrasts with other defects in semiconductors such as silicon where the formation energies of, e.g., the self-interstitial, strongly differ by about 1 eV between semilocal and hybrid functionals [75] with the hybrid functional agreeing with experiment and diffusion Monte Carlo calculations [76].

Experimental conditions such as the choice of synthesis and processing techniques, selection of precursors, precursor concentrations and partial pressures, substrates, and temperature all have a profound impact on the chemical potentials of the components, and hence the practical realization of doping in monolayer MoS_2 and related systems. The defect formation energies strongly depend on the components' chemical potentials, as evident from Eq. (1). The defect formation energies reported in Figs. 2 and 5 correspond to the Mo-rich/S-poor and Re/Nb-rich chemical potential limits. Under these conditions, the formation energies for the S vacancy, Re dopant, $Re_{Mo}V_S$, and $Nb_{Mo}V_S$ defect complexes are all greater than 1 eV, which suggests that their formation is unfavorable. However, an appropriate choice of experimental conditions, e.g., more S-rich conditions, can substantially reduce the formation energy for substitutional dopants on the Mo-site, such that it has been possible to achieve over 1 at.% Re doping in monolayer MoS_2 samples [32, 70]. However, care must be taken to avoid the formation of secondary phases, e.g., ReS_2, NbS_2, which also become more favorable under S-rich conditions; for example, Zhang *et al.* observed segregation of ReS_2 when they increased the precursor temperature during powder vaporization synthesis of Re-doped MoS_2 [32].

The concentrations of defects and dopants in real samples are also primarily influenced by non-equilibrium processes. The formation energy of the S vacancy is lowest in the Mo-rich/S-poor chemical potential limit considered in this work, corresponding to an equilibrium defect concentration of 10^{-8} to 10^{-7} at.% (10^{7} to 10^{8} cm^{-2}). However, S vacancy defect concentrations on the order of 10^{13} cm^{-2}, i.e., 10^{5} times higher than thermodynamic equilibrium concentrations, have been observed experimentally [49, 50], suggesting that the thermodynamic equilibrium chemical potential may not be the main driving force in determining the concentration of S vacancies. In practice, the formation of competing phases which should occur in equilibrium might be hindered by nucleation barriers, resulting in the local chemical potentials deviating significantly from that assumed in an equilibrium analysis.

It is important to note that while the defect formation energies depend on the chemical potentials, neither the CTLs nor complex binding energies do (see Eq. (3)). Therefore, the discussions and conclusions drawn based on the analysis of the CTLs and complex binding energies remain valid regardless of the choice of chemical potential references. The trends in the CTLs have been verified by the density of states calculations, which clearly do not depend on the chemical potentials. The chemical potentials may still indirectly influence the likelihood of complex formation by controlling the concentrations of the individual defects; however, the binding energy is independent of the chemical potentials.

The properties of 2D materials are strongly affected by their dielectric environment; hence the choice of substrate is key to achieving the desired electronic and optical properties in these doped systems. In this work, as a simplifying approximation, we have computed the properties of the dopants and defect complexes in a freestanding MoS_2 monolayer. However, in practice, substrates play essential roles in the syn-

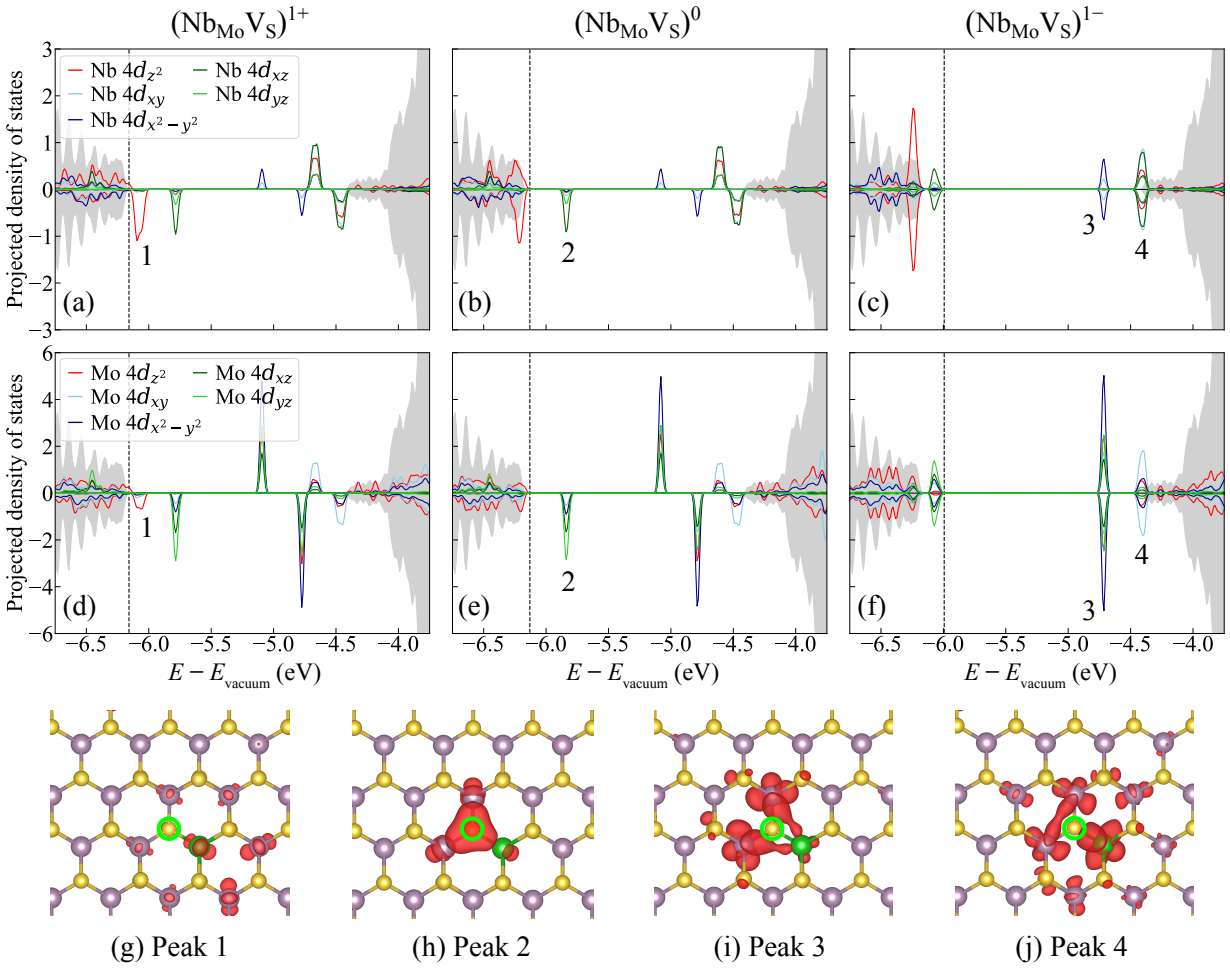

FIG. 7. Projected densities of states for the $Nb_{Mo}V_S$ defect complex in the +1, 0, and −1 charge states, calculated with the SCAN+rVV10 functional. The densities of states are projected onto the *d*-orbitals of the Nb substitutional dopant atom ((a) – (c)) and *d*-orbitals of the other two Mo atoms directly adjacent to the S vacancy ((d) – (f)). For comparison, the total density of states of pristine MoS_2 is shown in grey shading. The energies are plotted with respect to the vacuum energy, with the Fermi energy indicated by the vertical dashed line. The electronic orbitals corresponding to selected defect peaks marked "1" – "4" are depicted in (g) – (j). Purple, gold, and green atoms indicate Mo, S, and Nb atoms, respectively, while the bright green circle marks the position of the S vacancy.

thesis and device applications of 2D materials. Recent computational studies [77–79] demonstrate the effect of substrate screening on valence and conduction band edge positions and CTLs of defects and dopants. For example, a SiO_2 substrate is estimated to reduce the ionization energies of Re and Nb dopants in MoS_2 by 0.1-0.15 eV [77, 79], while a HfO_2 substrate could reduce them by up to 0.25 eV [77]. This general trend is attributed to the substrate dielectric screening helping to stabilize the charged states of these dopants, thereby making ionization more favorable and moving the CTLs closer to the corresponding bad edges. Therefore, even though our calculations of Re and Nb dopants in freestanding monolayer MoS_2 do not suggest them to be particularly shallow dopants, their doping effectiveness could be significantly enhanced in practice by a suitable choice of substrate.

The practical implications of our findings, especially as pertains to the defect complexes, are complex; they have the potential to be either detrimental or beneficial depending on the applications. For example, even though the formation of the dopant-vacancy complex appears to degrade the doping properties of Re in MoS_2, it could present opportunities for new technological applications such as single-photon emitters (SPE). Recently, based on first-principles electronic structure calculations, Gupta *et al.* [67] suggested that the neutral $Re_{Mo}V_S$ defect complex in MoS_2 could be a candidate SPE due to its paramagnetic spin doublet configuration, and the two-level quantum system formed by the majority spin-states, which are spatially localized and sufficiently isolated from the band edges. These features are borne out in our calculations as well, although further validation with a higher level of theory and experimental demonstration is still required.

The predicted range of the binding energy ΔE for the $Re_{Mo}V_S$ defect complex and its linear dependence on the Fermi level within the gap also presents an avenue for Fermi level control of active dopants and dopant-vacancy complexes. Varying the Fermi level from the VBM to the CBM tunes the

binding energy from ≈ -0.1 to almost -1 eV, which would increase the fraction of dopants in complexes from 0 to almost 100%. In practice, gating or the choice of substrates could potentially be used to control the Fermi level and, hence, the defect populations. Depending on the desired application, the Fermi level could be chosen to either minimize the number of defect complexes, i.e. maximize the number of active dopants for doping purposes, or maximize the number of defect complexes, e.g., to maximize the number of potential SPE. Such an approach for Fermi level control of dopants is made possible because the formation of the dopant-vacancy complex is a grand canonical process that involves the exchange of electrons with a charge reservoir. The prediction of this defect behavior, which could have compelling technological applications, is enabled by calculating the energy and electronic properties of the different charged states of each of the individual defects as well as the complex with the appropriate electrostatic boundary conditions provided by the charge correction scheme.

In contrast to the $Re_{Mo}V_S$ defect complex, our calculations of the $Nb_{Mo}V_S$ defect complex suggest that the Nb dopant and S vacancy do not have a strong tendency to form complexes, the binding energy shows little variation with the Fermi level, and the complex appears to maintain its acceptor character in MoS_2. These results suggest that the Nb dopant is more robust against compensation by S vacancies, the most common intrinsic defects in MoS_2. This could be encouraging for the prospect of *p*-type doping in MoS_2, which has thus far been more challenging to achieve than *n*-type doping.

VI. CONCLUSIONS

First-principles calculations for Re and Nb dopants in monolayer MoS_2 and their defect complexes with intrinsic S vacancies demonstrate the remarkably different behavior for these two dopants. We compute the formation energy of each dopant and complex in different charge states, utilizing the charge correction scheme of Freysoldt and Neugebauer to ensure the appropriate electrostatic boundary conditions for 2D materials. This approach enables the accurate prediction of the charge transition levels, the evaluation of the complex binding energies as a function of the Fermi level, and the characterization of their electronic properties. We show that Re dopants can form complexes with the S vacancies when the Fermi level approaches the CBM. These $Re_{Mo}V_S$ defect complexes quench the *n*-type doping of Re_{Mo} but could act as single-photon emitters. In contrast, Nb dopants are unlikely to form bound complexes with S vacancies, and their *p*-type doping properties appear to be less sensitive to the presence of S vacancies.

Our results illustrate how intricate the interactions between different dopants and defects can be, how greatly they differ between similar dopants and defects, and how they require the appropriate treatment of the electrostatic boundary conditions in 2D materials. This complexity highlights the need for further systematic, detailed, and extensive studies of defects, dopants, and complexes in 2D semiconductors, which will be crucial to realize the potential of 2D materials in next-generation technologies.

ACKNOWLEDGMENTS

This work was supported by the National Science Foundation through the 2DCC-MIP under award DMR-1539916 and by the awards DMR-1748464 and OAC-1740251. Computational resources were provided by the University of Florida Research Computing Center.

[1] K. F. Mak, C. Lee, J. Hone, J. Shan, and T. F. Heinz, Phys. Rev. Lett. **105**, 136805 (2010).
[2] B. Radisavljevic, A. Radenovic, J. Brivio, V. Giacometti, and A. Kis, Nat. Nanotech. **6**, 147 (2011).
[3] A. K. Geim and I. V. Grigorieva, Nature **499**, 419 (2013).
[4] S. Z. Butler, S. M. Hollen, L. Cao, Y. Cui, J. A. Gupta, H. R. Gutiérrez, T. F. Heinz, S. S. Hong, J. Huang, A. F. Ismach, E. Johnston-Halperin, M. Kuno, V. V. Plashnitsa, R. D. Robinson, R. S. Ruoff, S. Salahuddin, J. Shan, L. Shi, M. G. Spencer, M. Terrones, W. Windl, and J. E. Goldberger, ACS Nano **7**, 2898 (2013).
[5] H. L. Zhuang and R. G. Hennig, J. Phys. Chem. C **117**, 20440 (2013).
[6] H. L. Zhuang and R. G. Hennig, Phys. Rev. B **88**, 115314 (2013).
[7] D. Jariwala, V. K. Sangwan, L. J. Lauhon, T. J. Marks, and M. C. Hersam, ACS Nano **8**, 1102 (2014).
[8] H. Liu, A. T. Neal, Z. Zhu, Z. Luo, X. Xu, D. Tománek, and P. D. Ye, ACS Nano **8**, 4033 (2014).
[9] L. Li, Y. Yu, G. J. Ye, Q. Ge, X. Ou, H. Wu, D. Feng, X. H. Chen, and Y. Zhang, Nat. Nanotech. **9**, 372 (2014).
[10] F. Xia, H. Wang, D. Xiao, M. Dubey, and A. Ramasubramaniam, Nat. Photon. **8**, 899– (2014).
[11] S. Wu, S. Buckley, J. R. Schaibley, L. Feng, J. Yan, D. G. Mandrus, F. Hatami, W. Yao, J. V. cković, A. Majumdar, and X. Xu, Nature **520**, 69 (2015).
[12] Y. Ye, Z. J. Wong, X. Lu, X. Ni, H. Zhu, X. Chen, Y. Wang, and X. Zhang, Nat. Photon. **9**, 733 (2015).
[13] L. Cao, MRS Bulletin **40**, 592 (2015).
[14] A. K. Singh, K. Mathew, H. L. Zhuang, and R. G. Hennig, J. Phys. Chem. Lett. **6**, 1087 (2015).
[15] Z. Y. Al Balushi, K. Wang, R. K. Ghosh, R. A. Vilá, S. M. Eichfeld, J. D. Caldwell, X. Qin, Y.-C. Lin, P. A. DeSario, G. Stone, S. Subramanian, D. F. Paul, R. M. Wallace, S. Datta, J. M. Redwing, and J. A. Robinson, Nat. Mater. **15**, 1166 (2016).
[16] H. L. Zhuang and R. G. Hennig, Phys. Rev. B **93**, 054429

(2016).
[17] M. Ashton, J. Paul, S. B. Sinnott, and R. G. Hennig, Phys. Rev. Lett. **118**, 106101 (2017).
[18] J. T. Paul, A. K. Singh, Z. Dong, H. Zhuang, B. C. Revard, B. Rijal, M. Ashton, A. Linscheid, M. Blonsky, D. Gluhovic, J. Guo, and R. G. Hennig, J. Phys.: Condens. Matter **29**, 473001 (2017).
[19] O. Lopez-Sanchez, D. Lembke, M. Kayci, A. Radenovic, and A. Kis, Nat. Nanotechnol. **8**, 497 (2013).
[20] H. L. Zhuang, M. D. Johannes, A. K. Singh, and R. G. Hennig, Phys. Rev. B **96**, 165305 (2017).
[21] L. Li, Z. Qin, L. Ries, S. Hong, T. Michel, J. Yang, C. Salameh, M. Bechelany, P. Miele, D. Kaplan, M. Chhowalla, and D. Voiry, ACS Nano **13**, 6824 (2019).
[22] H. Li, G. Lu, Z. Yin, Q. He, H. Li, Q. Zhang, and H. Zhang, Small **8**, 682 (2012).
[23] Y.-H. Lee, X.-Q. Zhang, W. Zhang, M.-T. Chang, C.-T. Lin, K.-D. Chang, Y.-C. Yu, J. T.-W. Wang, C.-S. Chang, L.-J. Li, and T.-W. Lin, Adv. Mater. **24**, 2320 (2012).
[24] S. McDonnell, R. Addou, C. Buie, R. M. Wallace, and C. L. Hinkle, ACS Nano **8**, 2880 (2014).
[25] M. M. Ugeda, A. J. Bradley, S.-F. Shi, F. H. da Jornada, Y. Zhang, D. Y. Qiu, W. Ruan, S.-K. Mo, Z. Hussain, Z.-X. Shen, F.Wang, S. G. Louie, and M. F. Crommie, Nat. Mater. **13**, 1091 (2014).
[26] J. Mann, D. Sun, Q. Ma, J.-R. Chen, E. Preciado, T. Ohta, B. Diaconescu, K. Yamaguchi, T. Tran, M. Wurch, K. Magnone, T. F. Heinz, G. L. Kellogg, R. Kawakami, and L. Bartels, Eur. Phys. J. B **86**, 226 (2013).
[27] K. Dolui, I. Rungger, and S. Sanvito, Phys. Rev. B **87**, 165402 (2013).
[28] A. Singh and A. K. Singh, Phys. Rev. B **99**, 121201(R) (2019).
[29] K. Zhang and J. Robinson, MRS Advances **4**, 2743 (2019).
[30] K. K. Tiong, Y. S. Huang, and C. H. Ho, J. Alloys Compd. **317–318**, 208 (2001).
[31] F. L. Deepak, R. Popovitz-Brio, Y. Feldman, H. Cohen, A. Enyashin, G. Seifert, and R. Tenne, Chem. Asian. J. **3**, 1568 (2008).
[32] K. Zhang, B. M. Bersch, J. Joshi, R. Addou, C. R. Cormier, C. Zhang, K. Xu, N. C. Briggs, K. Wang, S. Subramanian, K. Cho, S. Fullerton-Shirey, R. M. Wallace, P. M. Vora, and J. A. Robinson, Adv. Funct. Mater. **28**, 1706950 (2018).
[33] J. Gao, Y. D. Kim, L. Liang, J. C. Idrobo, P. Chow, J. Tan, B. Li, L. Li, B. G. Sumpter, T.-M. Lu, V. Meunier, J. Hone, and N. Koratkar, Adv. Mater. **28**, 9735 (2016).
[34] J. Suh, T.-E. Park, D.-Y. Lin, D. Fu, J. Park, H. J. Jung, Y. Chen, C. Ko, C. Jang, Y. Sun, R. Sinclair, J. Chang, S. Tongay, and J. Wu, Nano Lett. **14**, 6976 (2014).
[35] M. R. Laskar, D. N. Nath, L. Ma, E. W. Lee II, C. H. Lee, T. Kent, Z. Yang, R. Mishra, M. A. Roldan, J.-C. Idrobo, S. T. Pantelides, S. J. Pennycook, R. C. Myers, Y. Wu, and S. Rajan, Appl. Phys. Lett. **104**, 092104 (2014).
[36] Y. Kim, H. Bark, B. Kang, and C. Lee, ACS Appl. Mater. Interfaces **11**, 12613 (2019).
[37] M. Li, J. Yao, X. Wu, S. Zhang, B. Xing, X. Niu, X. Yan, Y. Yu, Y. Liu, and Y. Wang, ACS Appl. Mater. Interfaces **12**, 6276 (2020).
[38] J. Neugebauer and C. G. Van de Walle, Appl. Phys. Lett. **69**, 503 (1996).
[39] T. Mattila and R. M. Nieminen, Phys. Rev. B **55**, 9571 (1997).
[40] F. A. Reboredo and S. T. Pantelides, Phys. Rev. Lett. **82**, 1887 (1999).
[41] C. G. Van de Walle and J. Neugebauer, J. Appl. Phys. **95**, 3851 (2004).
[42] Q. Yan, A. Janotti, M. Scheffler, and C. G. Van de Walle, Appl. Phys. Lett. **100**, 142110 (2012).
[43] N. A. Richter, F. Stavale, S. V. Levchenko, N. Nilius, H.-J. Freund, and M. Scheffler, Phys. Rev. B **91**, 195305 (2015).
[44] J.-Y. Noh, H. Kim, and Y.-S. Kim, Phys. Rev. B **89**, 205417 (2014).
[45] H.-P. Komsa and A. V. Krasheninnikov, Phys. Rev. B **91**, 125304 (2015).
[46] S. Haldar, H. Vovusha, M. K. Yadav, O. Eriksson, and B. Sanyal, Phys. Rev. B **92**, 235408 (2015).
[47] H.-P. Komsa, J. Kotakoski, S. Kurasch, O. Lehtinen, U. Kaiser, and A. V. Krasheninnikov, Phys. Rev. Lett. **109**, 035503 (2012).
[48] W. Zhou, X. Zou, S. Najmaei, Z. Liu, Y. Shi, J. Kong, J. Lou, P. M. Ajayan, B. I. Yakobson, and J.-C. Idrobo, Nano Lett. **13**, 2615 (2013).
[49] J. Hong, Z. Hu, M. Probert, K. Li, D. Lv, X. Yang, L. Gu, N. Mao, Q. Feng, L. Xie, J. Zhang, D. Wu, Z. Zhang, C. Jin, W. Ji, X. Zhang, J. Yuan, and Z. Zhang, Nat. Commun. **6**, 6293 (2015).
[50] P. Vancsó, G. Z. Magda, J. Pető, J.-Y. Noh, Y.-S. Kim, C. Hwang, L. P. Biró, and L. Tapasztó, Sci. Rep. **6**, 29726 (2016).
[51] A. M. Z. Tan, C. Freysoldt, and R. G. Hennig, Phys. Rev. Mater. **4**, 064004 (2020).
[52] P. Zhao, J. Zheng, P. Guo, Z. Jiang, L. Cao, and Y. Wan, Comp. Mat. Sci. **128**, 287 (2017).
[53] Y. Lin, D. O. Dumcenco, H.-P. Komsa, Y. Niimi, A. V. Krasheninnikov, Y. Huang, and K. Suenaga, Adv. Mater. **26**, 2857 (2014).
[54] G. Kresse and J. Furthmüller, Phys. Rev. B **54**, 11169 (1996).
[55] P. E. Blöchl, Phys. Rev. B **50**, 17953 (1994).
[56] G. Kresse and D. Joubert, Phys. Rev. B **59**, 1758 (1999).
[57] J. P. Perdew, K. Burke, and M. Ernzerhof, Phys. Rev. Lett. **77**, 3865– (1996).
[58] J. Sun, A. Ruzsinszky, and J. P. Perdew, Phys. Rev. Lett. **115**, 036402 (2015).
[59] J. Heyd, G. Scuseria, and M. Ernzerhof, J. Chem. Phys. **118**, 8207 (2003).
[60] J. Heyd, G. Scuseria, and M. Ernzerhof, J. Chem. Phys. **124**, 219906 (2006).
[61] H. Peng, Z.-H. Yang, J. P. Perdew, and J. Sun, Phys. Rev. X **6**, 041005 (2016).
[62] M. Methfessel and A. T. Paxton, Phys. Rev. B **40**, 3616 (1989).
[63] H. J. Monkhorst and J. D. Pack, Phys. Rev. B **13**, 5188– (1976).
[64] C. Freysoldt, B. Grabowski, T. Hickel, J. Neugebauer, G. Kresse, A. Janotti, and C. G. Van de Walle, Rev. Mod. Phys. **86**, 253 (2014).
[65] C. Freysoldt and J. Neugebauer, Phys. Rev. B **97**, 205425 (2018).
[66] C. Freysoldt, P. Eggert, P. Rinke, A. Schindlmayr, and M. Scheffler, Phys. Rev. B **77**, 235428 (2008).
[67] S. Gupta, J.-H. Yang, and B. I. Yakobson, Nano Lett. **19**, 408 (2019).
[68] H.-P. Komsa, S. Kurasch, O. Lehtinen, U. Kaiser, and A. V. Krasheninnikov, Phys. Rev. B **88**, 035301 (2013).
[69] M. G. Sensoy, D. Vinichenko, W. Chen, C. M. Friend, and E. Kaxiras, Phys. Rev. B **95**, 014106 (2017).
[70] Z. Wang, G. Zhao, R. Luo, I. Johnson, H. Kashani, and M. Chen, Phys. Rev. B **100**, 085401 (2019).
[71] K. Dolui, I. Rungger, C. Das Pemmaraju, and S. Sanvito, Phys. Rev. B **88**, 075420 (2013).
[72] B. Schuler, J.-H. Lee, C. Kastl, K. A. Cochrane, C. T. Chen, S. Refaely-Abramson, S. Yuan, E. van Veen, R. Roldán, N. J. Borys, R. J. Koch, S. Aloni, A. M. Schwartzberg, D. F. Ogle-

tree, J. B. Neaton, and A. Weber-Bargioni, ACS Nano **13**, 10520 (2019).
[73] A. Alkauskas and A. Pasquarello, Phys. Rev. B **84**, 125206 (2011).
[74] C. Freysoldt, B. Lange, J. Neugebauer, Q. Yan, J. L. Lyons, A. Janotti, and C. G. Van de Walle, Phys. Rev. B **93**, 165206 (2016).
[75] E. R. Batista, J. Heyd, R. G. Hennig, B. P. Uberuaga, R. L. Martin, G. E. Scuseria, C. J. Umrigar, and J. W. Wilkins, Phys. Rev. B **74**, 121102(R) (2006).
[76] W. D. Parker, J. W. Wilkins, and R. G. Hennig, Phys. Status Solidi B **248**, 267 (2011).
[77] J.-Y. Noh, H. Kim, M. Park, and Y.-S. Kim, Phys. Rev. B **92**, 115431 (2015).
[78] M. H. Naik and M. Jain, Phys. Rev. Mater. **2**, 084002 (2018).
[79] D. Wang and R. Sundararaman, Phys. Rev. Mater. **3**, 083803 (2019).